

Figure 1

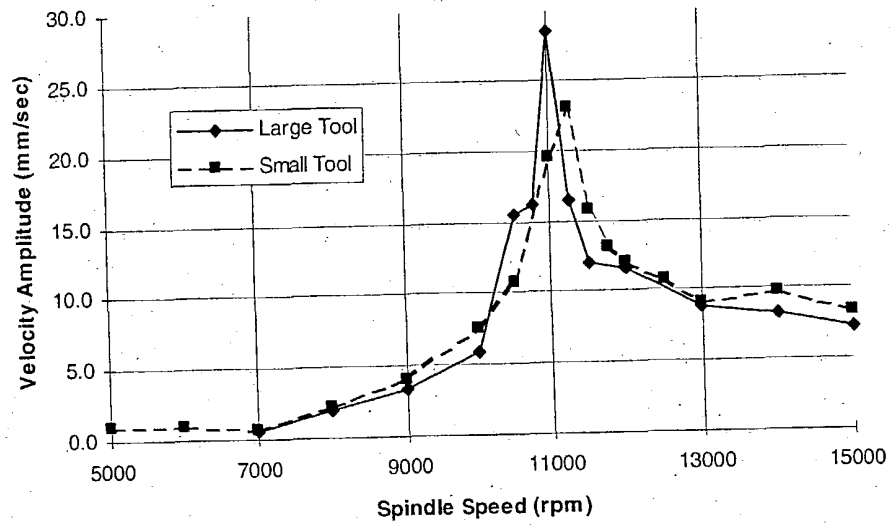


Figure 2 Vibration Sensitivity of MFW2612/15 Spindle To Maximum Capacity Balance Correction

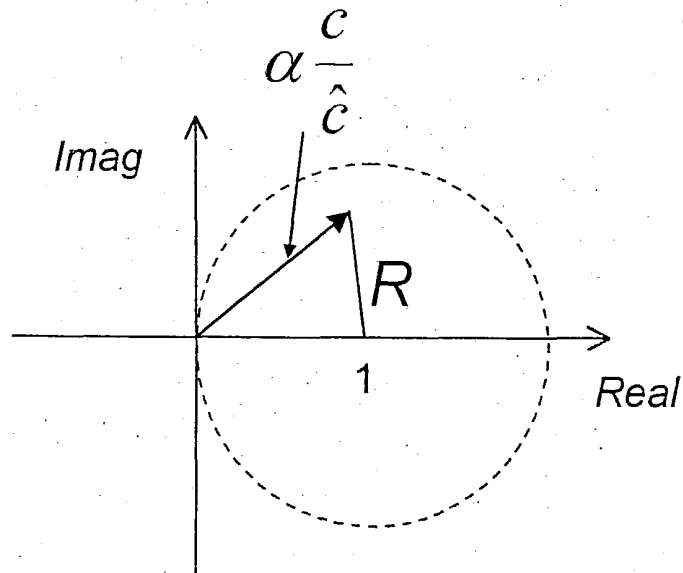


Figure 3.1 Single-Plane Active Balancing Control Stable For All Values of $\alpha \frac{c}{\hat{c}}$ Falling Within the Unit Circle In The Right Half Complex Plane ($R < 1$)

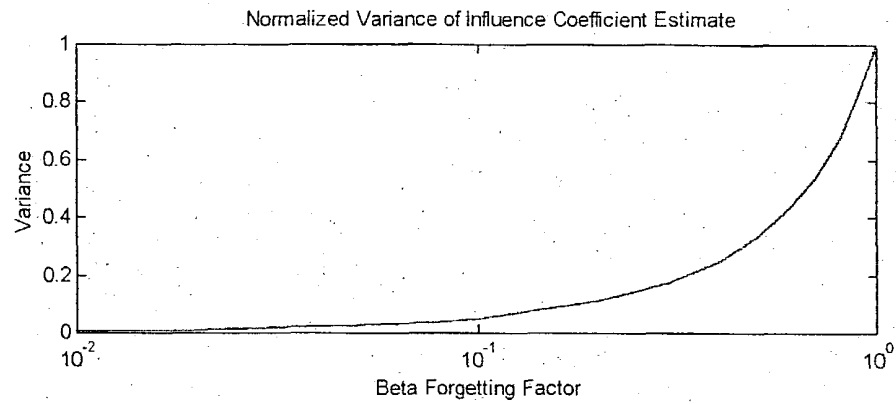


Figure 3.2 Beta Forgetting Factor with a Normalized Variance of Coefficient Estimate

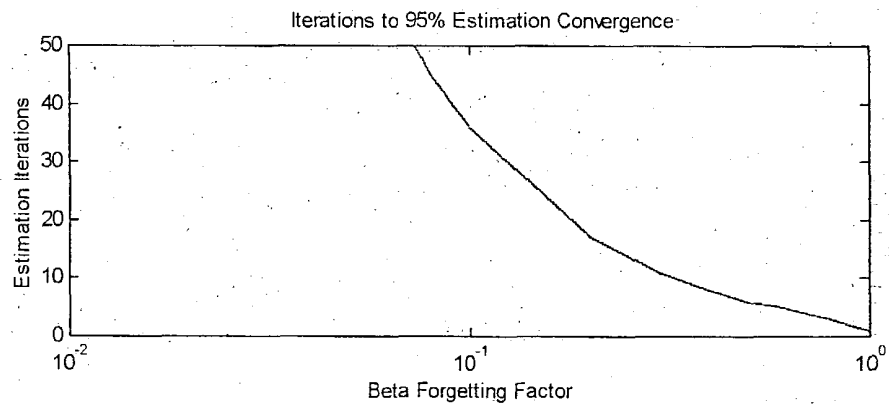


Figure 3.3 Influence Coefficient Estimation Performance for Various Values of the β "Forgetting Factor"

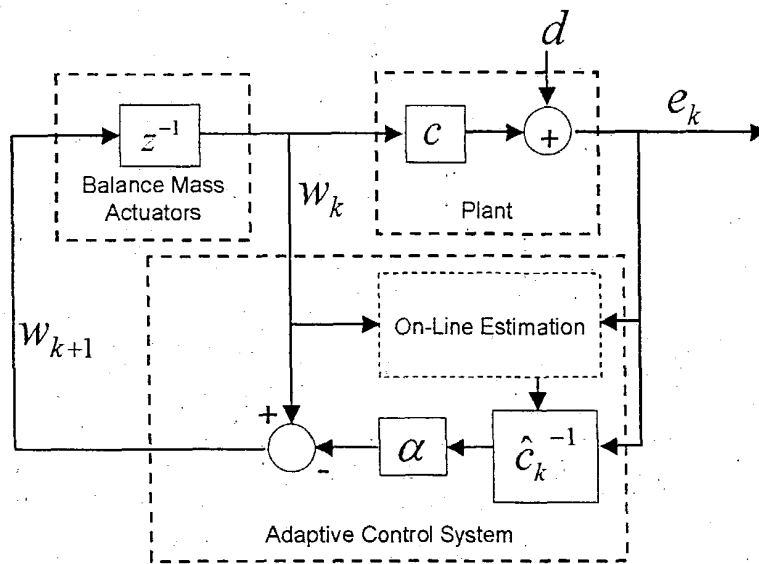


Figure 3.4 Adaptive Influence Coefficient Control Block Diagram

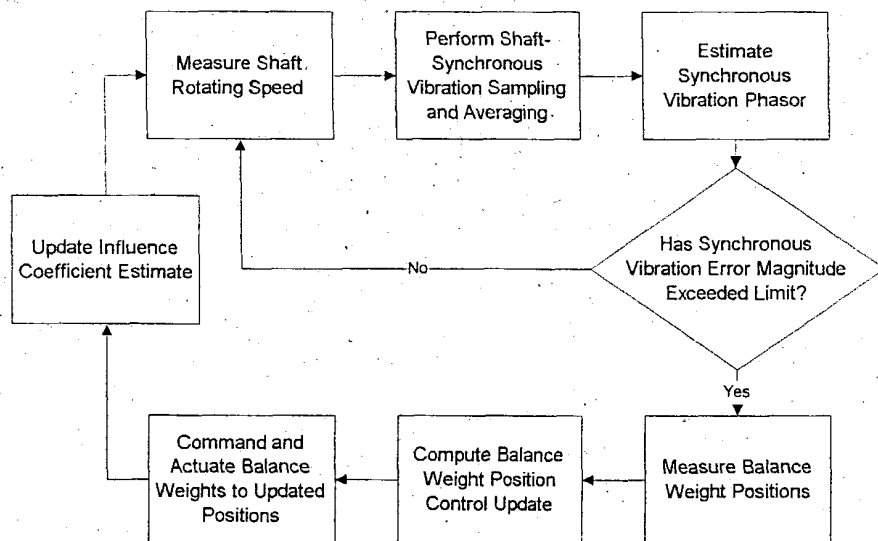


Figure 3.5 Flow Chart of Experimental Single-Plane Active Balancing Control System

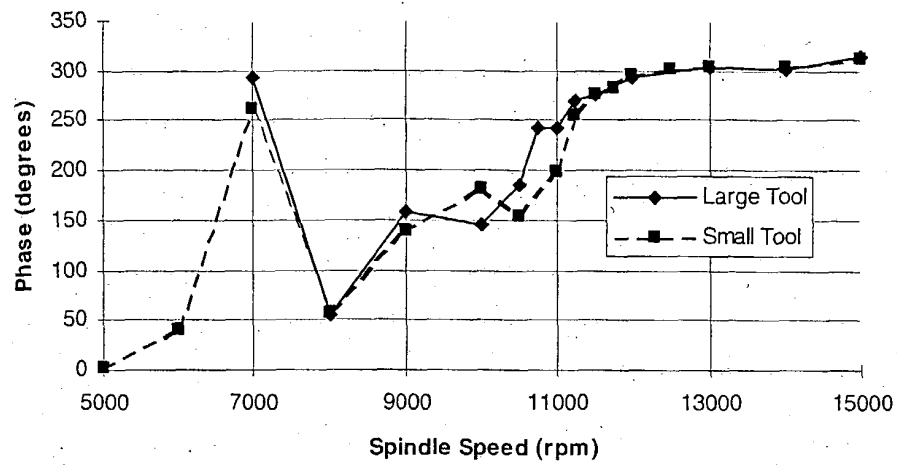


Figure 3.6 Vibration Sensitivity Phase Angle of MFW2612/15 Spindle

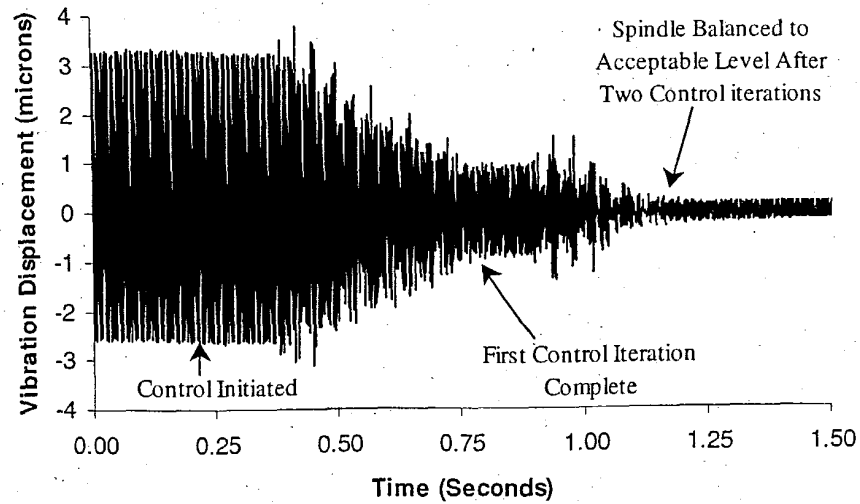


Figure 3.7 Measured Spindle Housing Vibration During Active Balancing of Nonlinear System

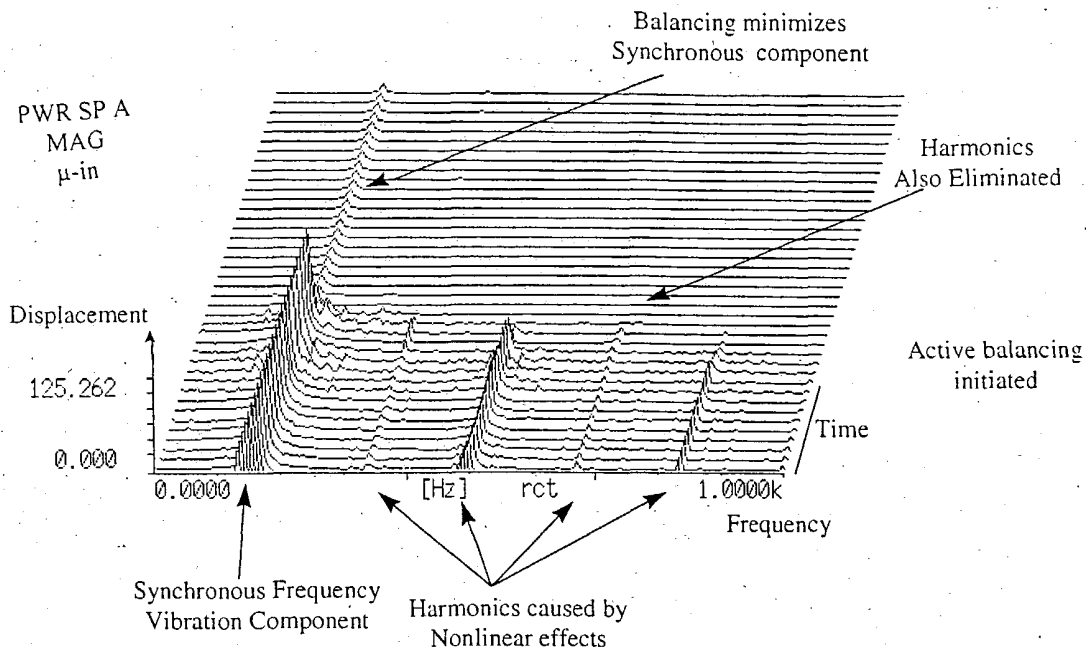


Figure 3.8 Measured Time-Frequency Spectrum of Spindle Housing Vibration Showing Broadband Effect of Active Balancing of Nonlinear System

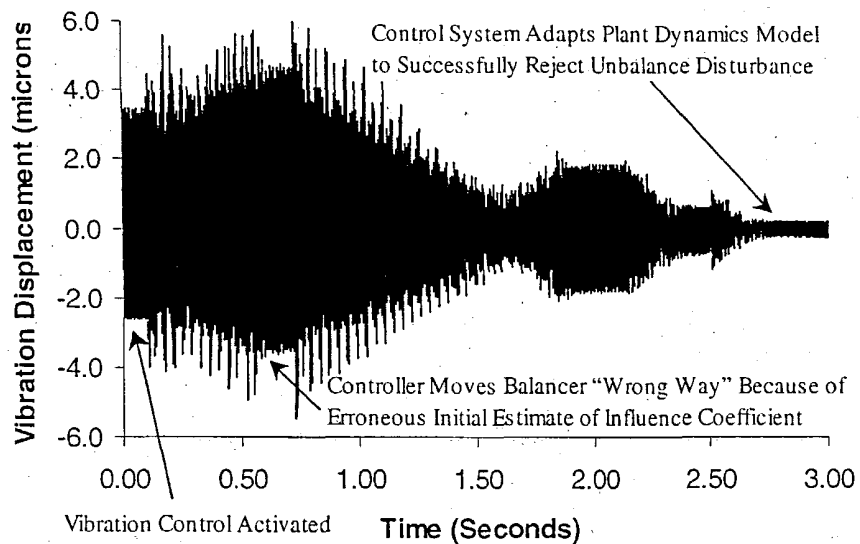


Figure 3.9 Measured Spindle Housing Vibration During Single-Plane Adaptive Active Balancing With Inaccurate Initial Influence Coefficient Estimate

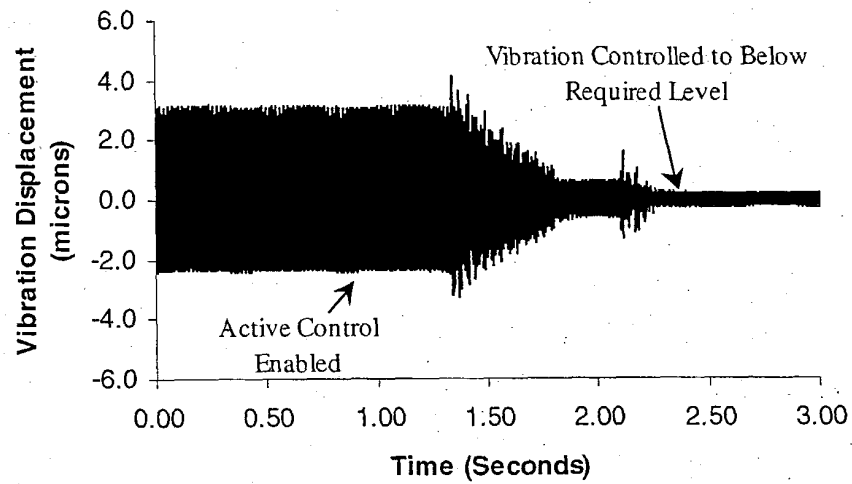


Figure 3.10 Measured Spindle Housing Vibration During Single-Plane Active Balancing After Adaptive System "Learning"

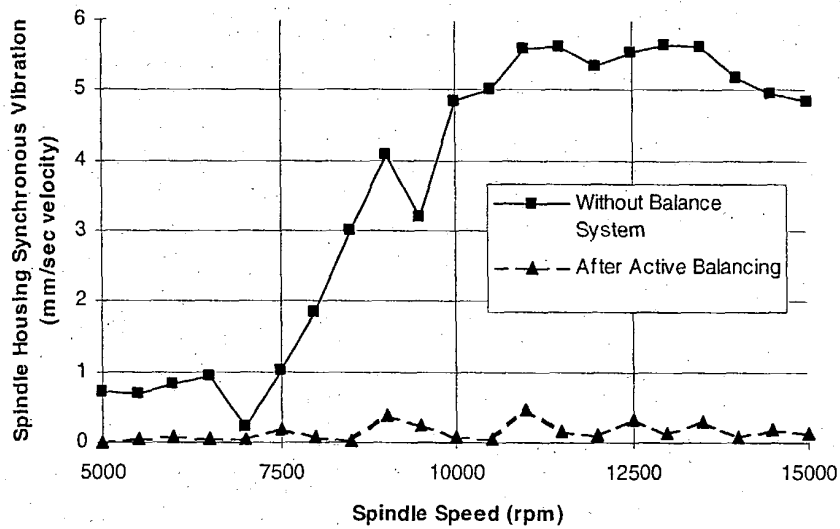


Figure 3.11 Measured Spindle Vibration Before and After Adaptive Active Balancing at Various Spindle Speeds

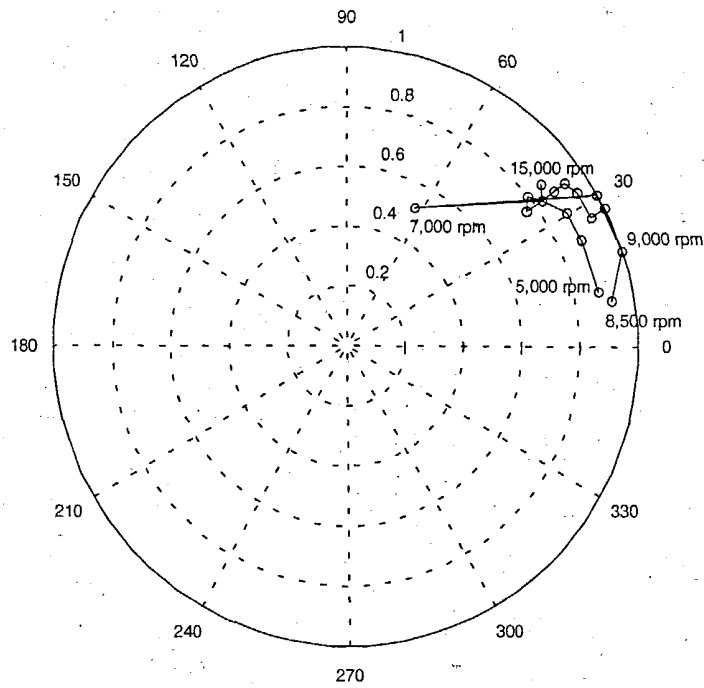


Figure 3.12 Normalized Magnitude and Phase of Balance Correction Required to Minimize Vibration at Each Spindle Speed

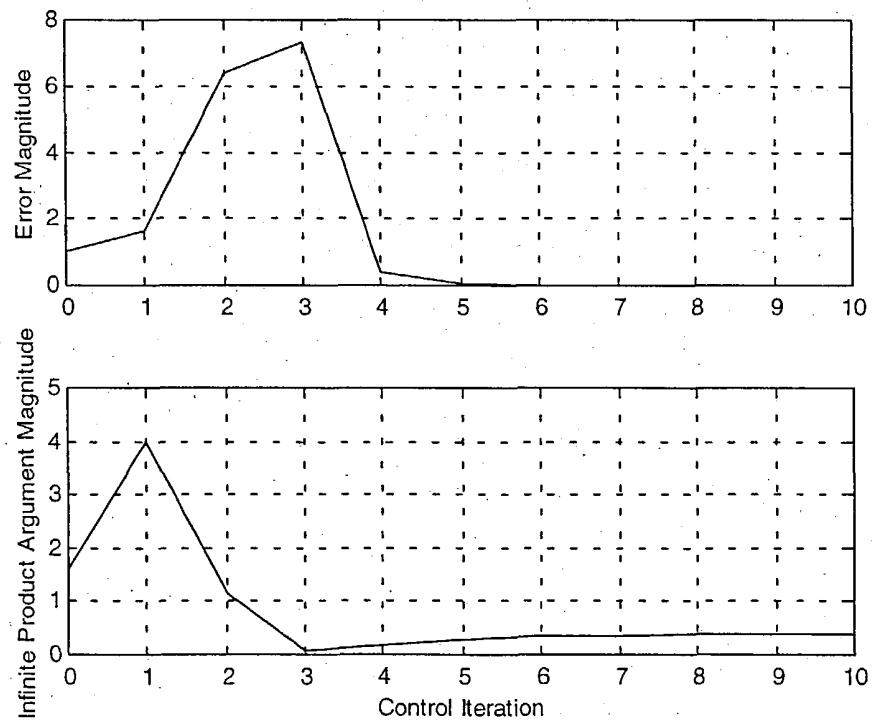


Figure 4.1 Example Simulated Adaptive Control Response and Infinite Product Argument Magnitude of Eq. (4.2) For $\hat{c}_0 = -c$, $\alpha = 0.6$, and $\beta = 0.4$

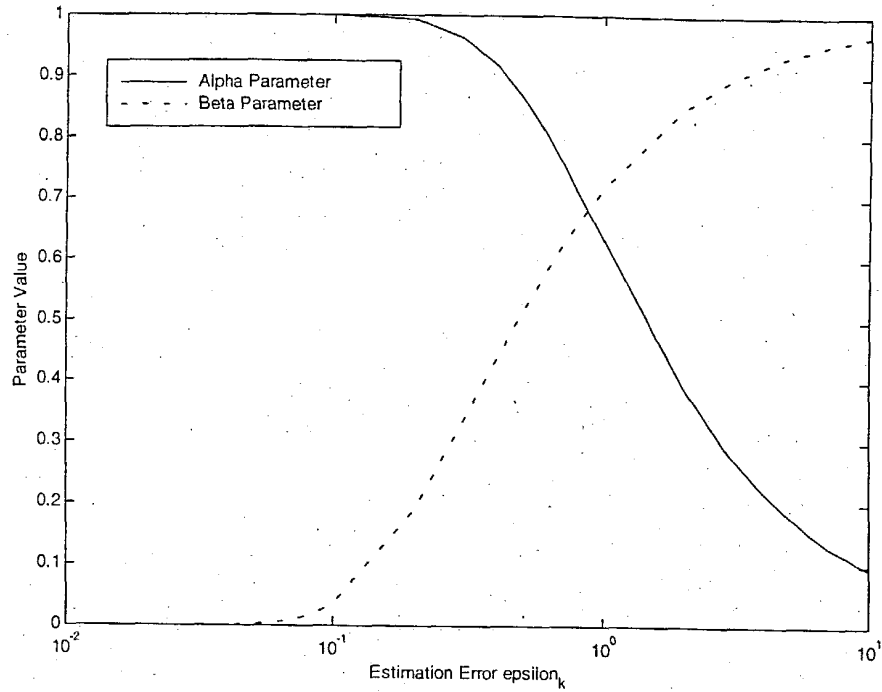


Figure 4.2 Automatically Tuned Parameter Values as Functions of Influence Coefficient Estimation Convergence Error (for $\eta_\alpha = 1$, and $\eta_\beta = 3$)

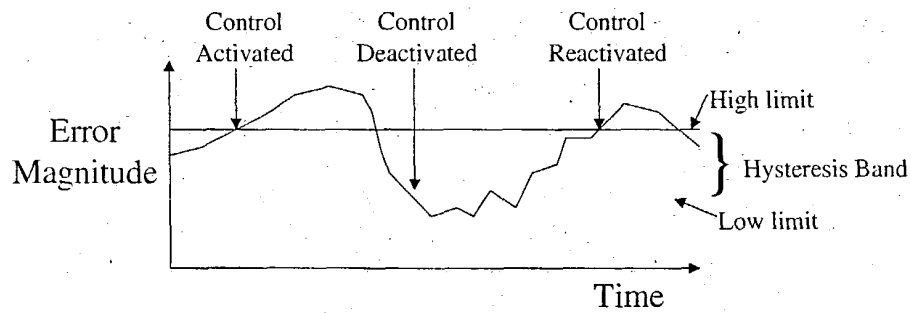


Figure 4.3 Hysteresis Band Between the Supervisory Limits Reduces Spurious Control Activation

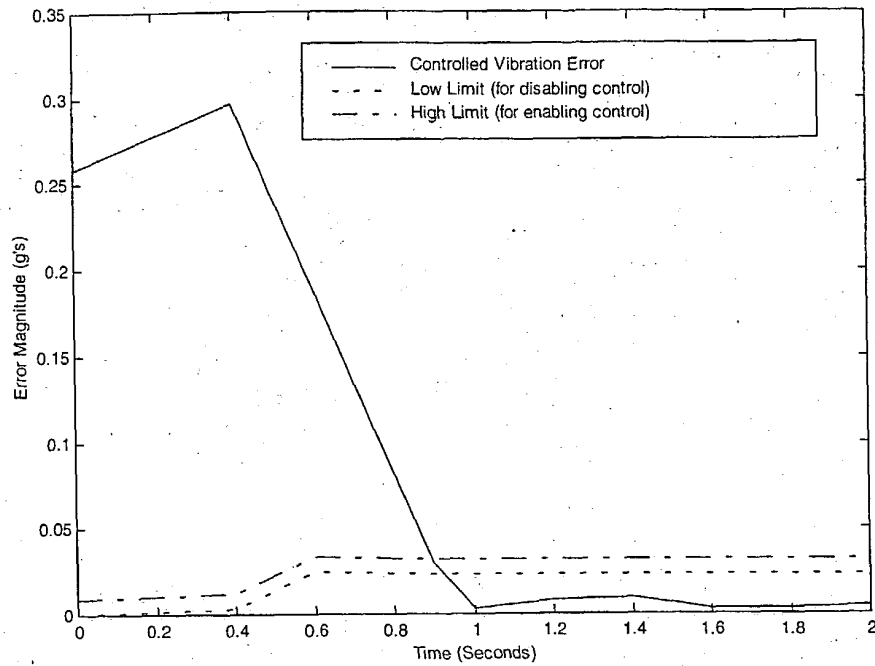


Figure 4.4 Experimental Results Using Automatic Supervisory Control Limit Setting With Auto-Tuning Active Balancing System

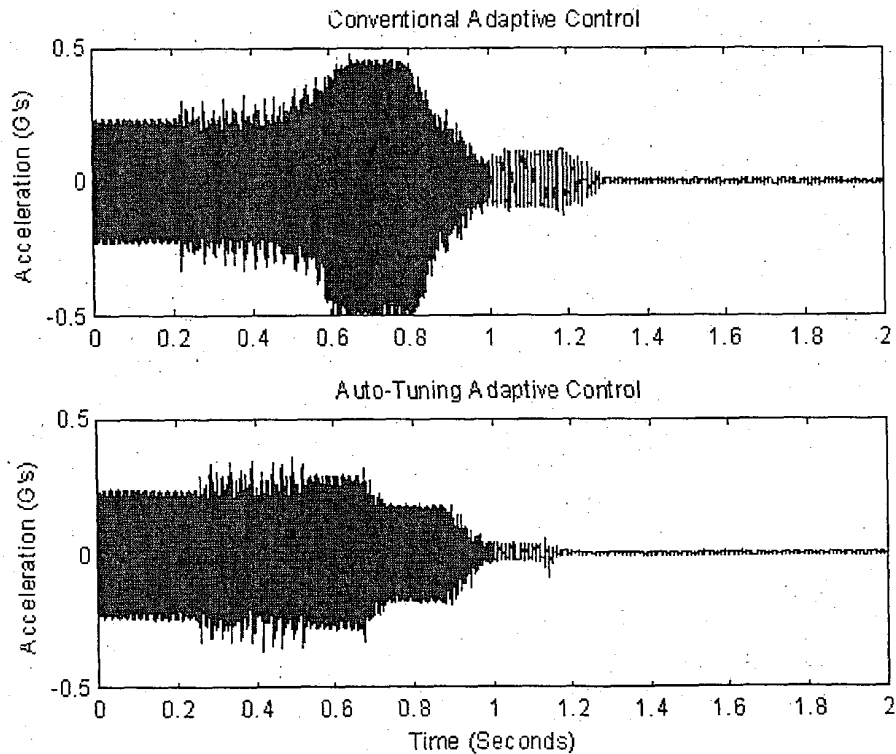


Figure 4.5 Spindle Housing Vibration During Active Balancing Using Conventional Fixed Parameter Adaptive Control and Auto-Tuning Adaptive Control With Erroneous Initial Influence Coefficient Estimates

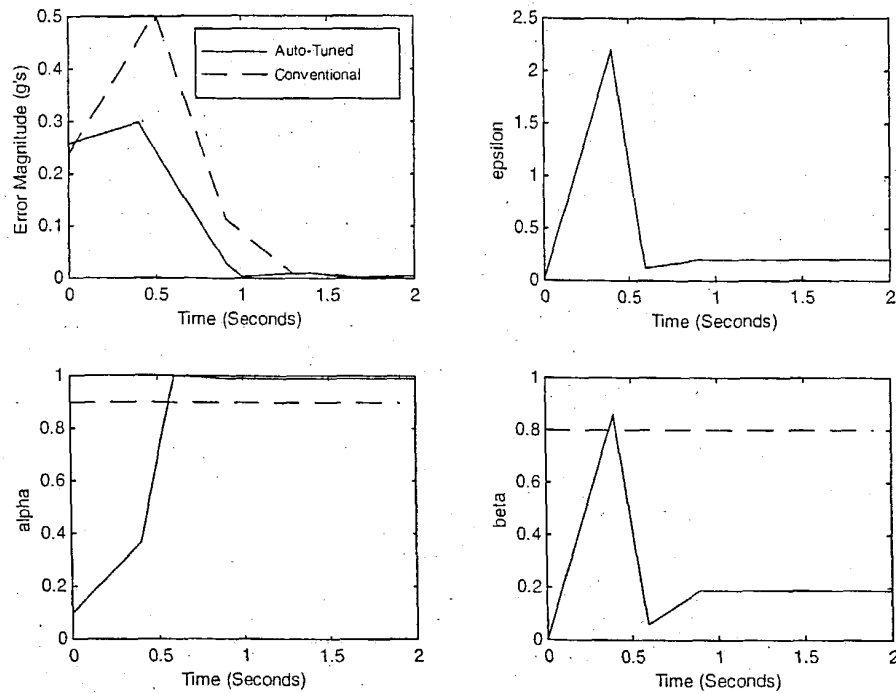


Figure 4.6 Comparison of Active Balancing Control Performance of Auto-Tuning Control and Conventional Fixed Parameter Adaptive Control With Erroneous Initial Influence Estimates

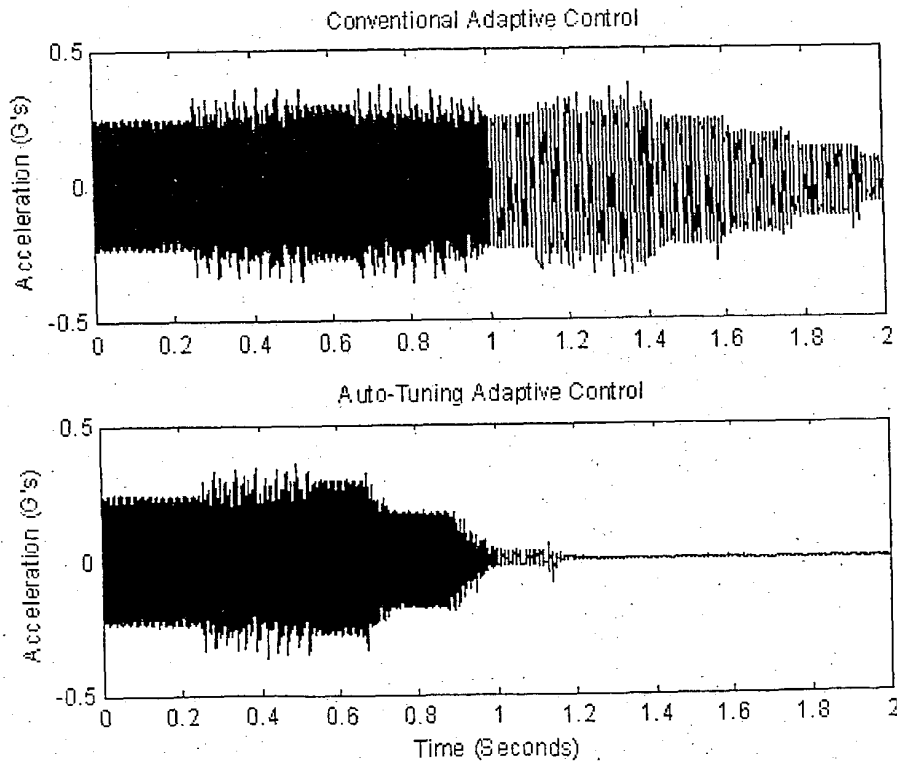


Figure 4.7 Spindle Housing Vibration During Active Balancing Using Cautious Conventional Fixed-Parameter Adaptive Control and Auto-Tuning Adaptive Control With Erroneous Initial Influence Coefficient Estimates

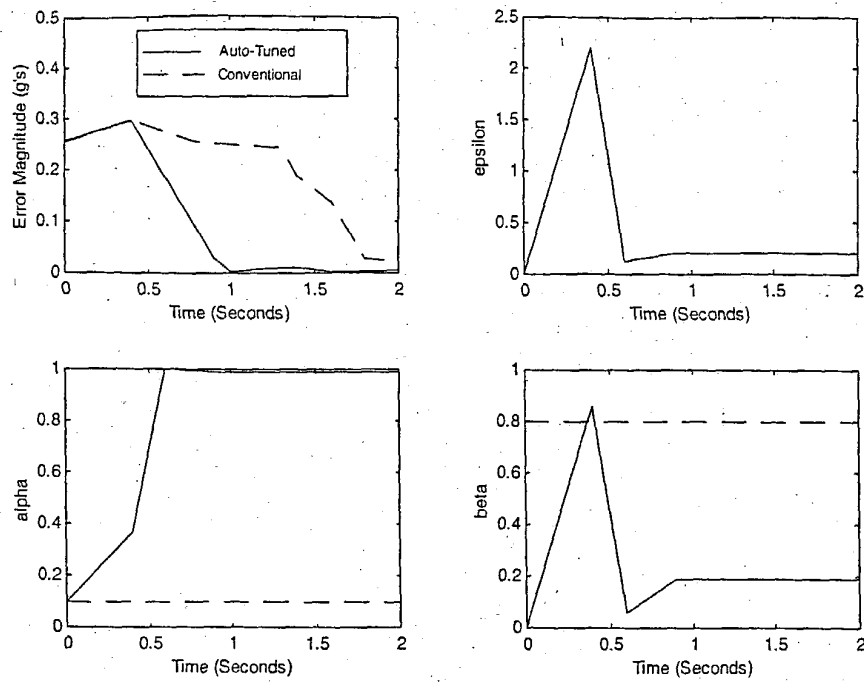


Figure 4.8 Comparison of Active Balancing Control Performance Using Cautious Conventional Fixed-Parameter Adaptive Control Auto-Tuning Control and With Erroneous Initial Influence Estimates

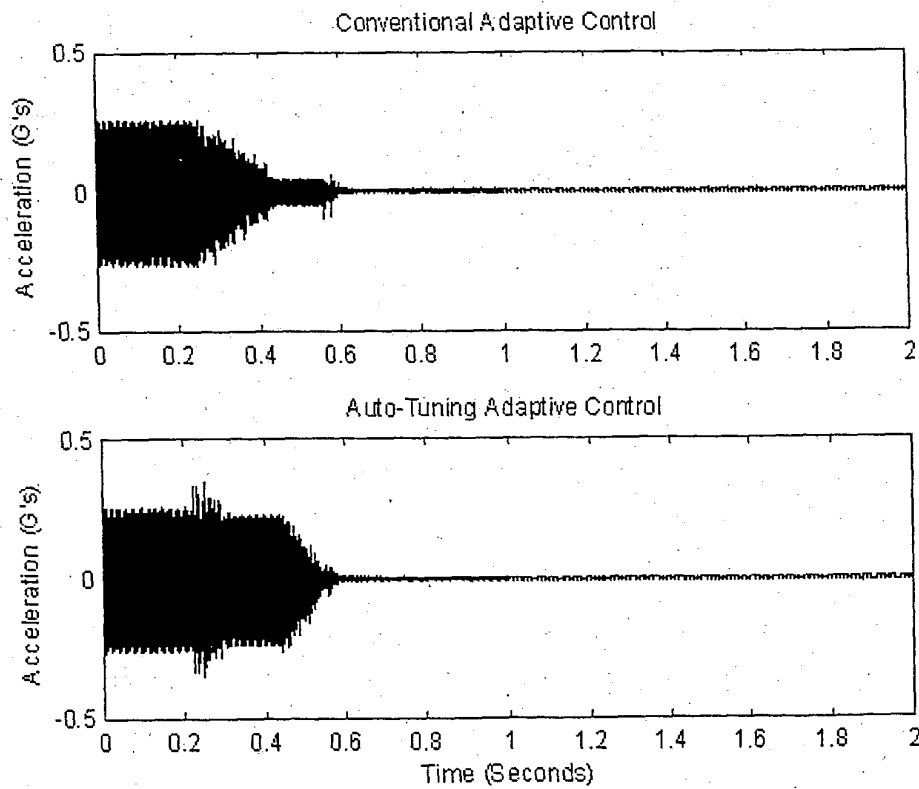


Figure 4.9 Spindle Housing Vibration During Active Balancing Using Conventional Adaptive Control and Auto-Tuning Adaptive Control With Accurate Initial Influence Coefficient Estimates

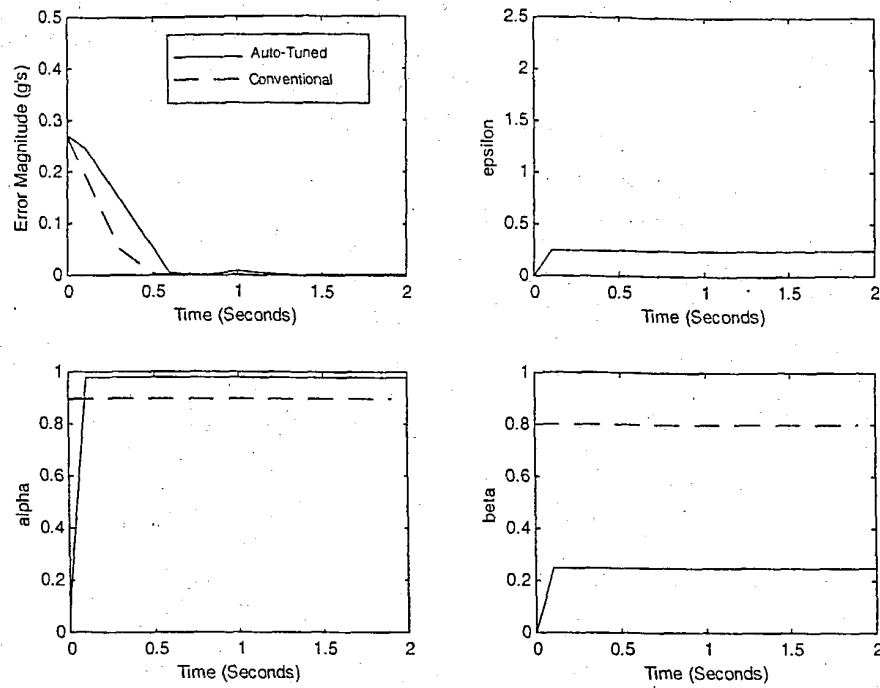


Figure 4.10 Comparison of Active Balancing Control Performance of Conventional Fixed-Parameter Adaptive and Control Auto-Tuning Control With Accurate Initial Influence Coefficient Estimates

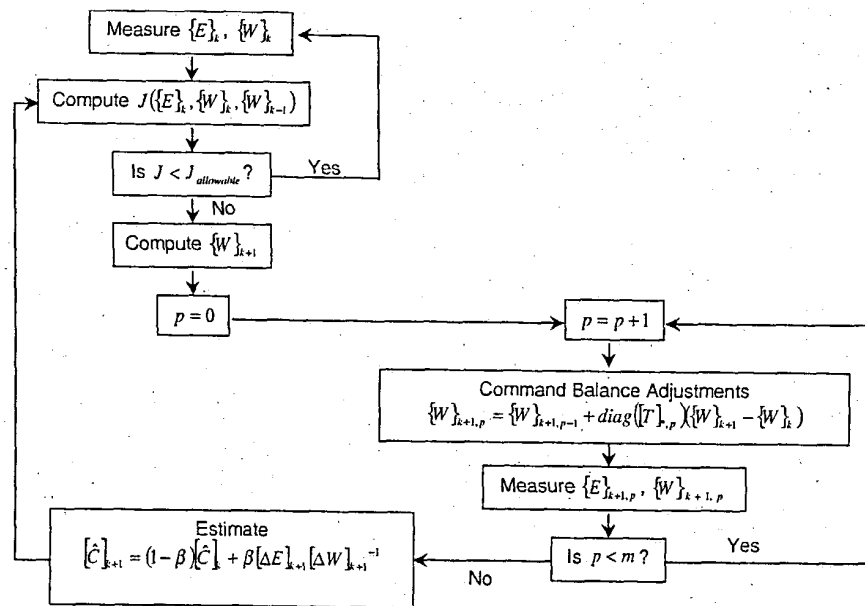


Figure 5.1 Flow Chart of Supervisory Adaptive Optimal Control for Multiple-Plane Active Balancing Systems

Figure 5.2 Average Measured Active Balancing Influence Matrix At 3,100 Rpm (Influence Units Are Mils Peak-To-Peak Per 100% Balance Capacity)

Sensor	Influence (mils p - p)	Active Balance Plane
$\begin{Bmatrix} \text{Drive End}_y \\ \text{Outboard}_y \\ \text{Drive End}_x \\ \text{Outboard}_x \end{Bmatrix}$	$\begin{bmatrix} 1.2\angle 178^\circ & 4.2\angle 228^\circ \\ 4.9\angle 343^\circ & 1.3\angle 152^\circ \\ 1.0\angle 152^\circ & 5.2\angle 142^\circ \\ 4.2\angle 78^\circ & 1.4\angle 226^\circ \end{bmatrix}$	$\begin{Bmatrix} \text{Drive End} \\ \text{Outboard} \end{Bmatrix}$

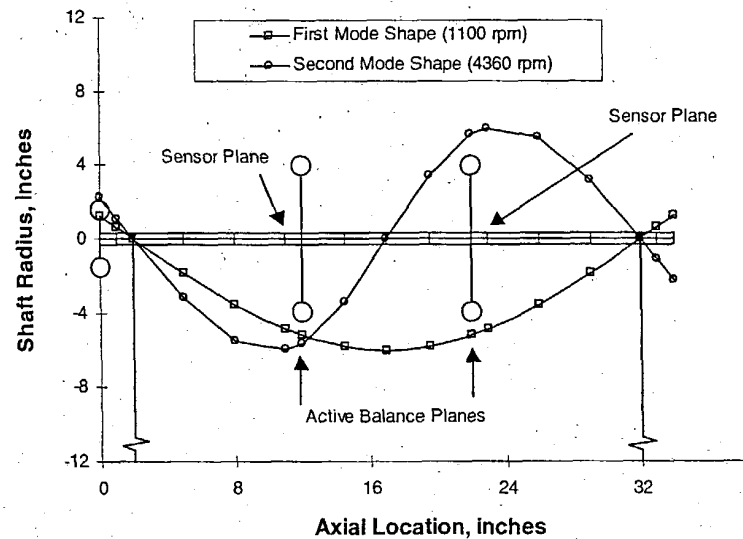


Figure 5.3 Predicted Mode Shapes of Flexible Rotor Test Rig for First Two Critical Speeds

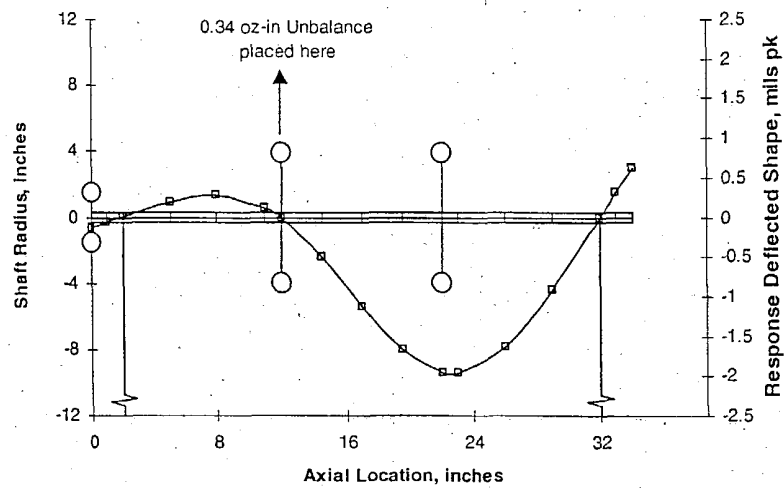


Figure 5.4 Predicted Forced Response Deflected Shape Of Rotor At 3,100 Rpm Due To 0.34 Oz-In Unbalance At Drive-End Active Balancing Plane

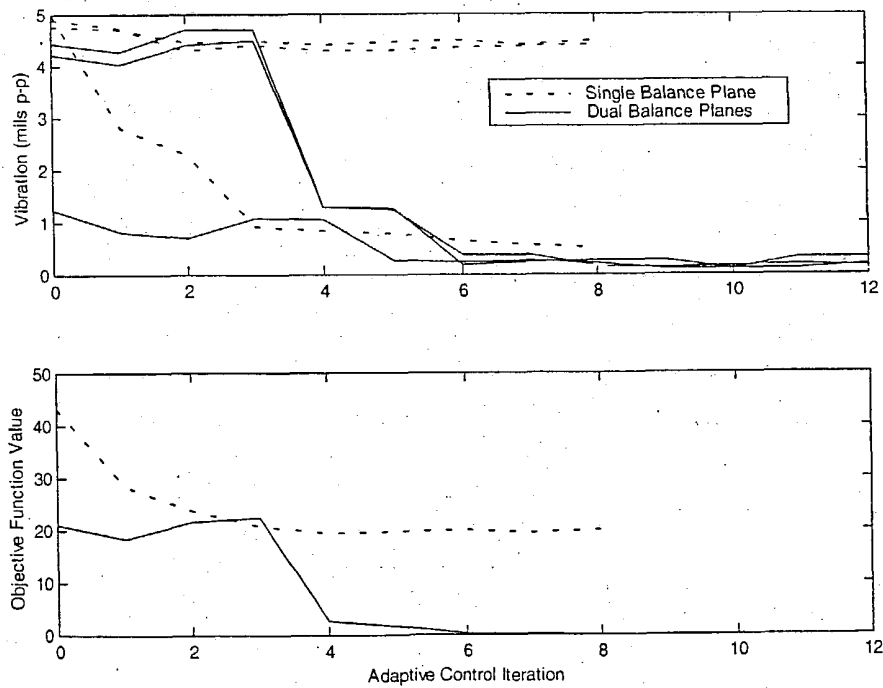


Figure 5.5 Comparison of Adaptive Optimal Control Results Using Single-Plane and Dual-Plane Active Balancing

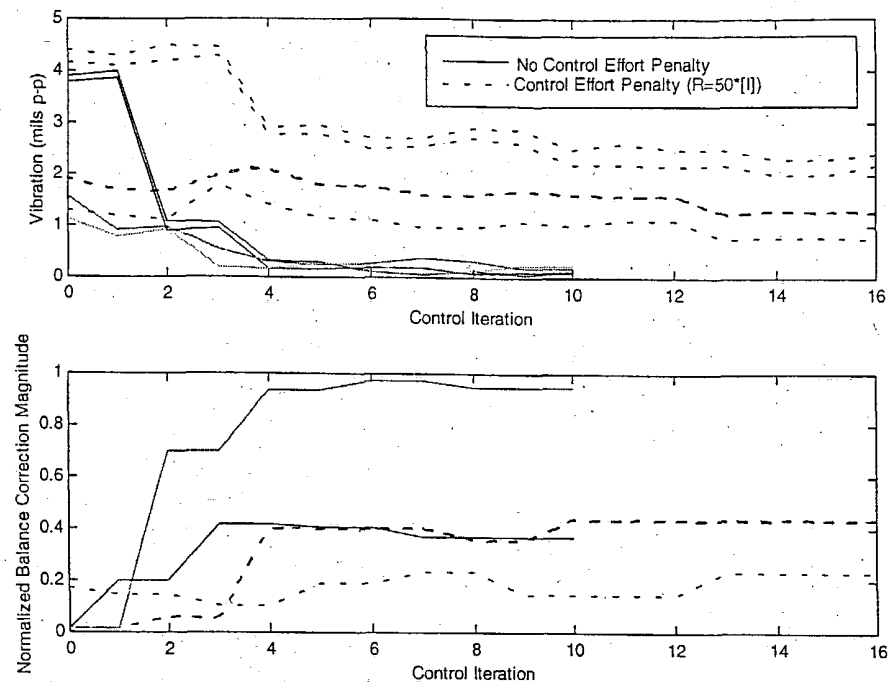


Figure 5.6 Comparative Results of Adaptive Optimal Control With and Without Control Effort Penalty

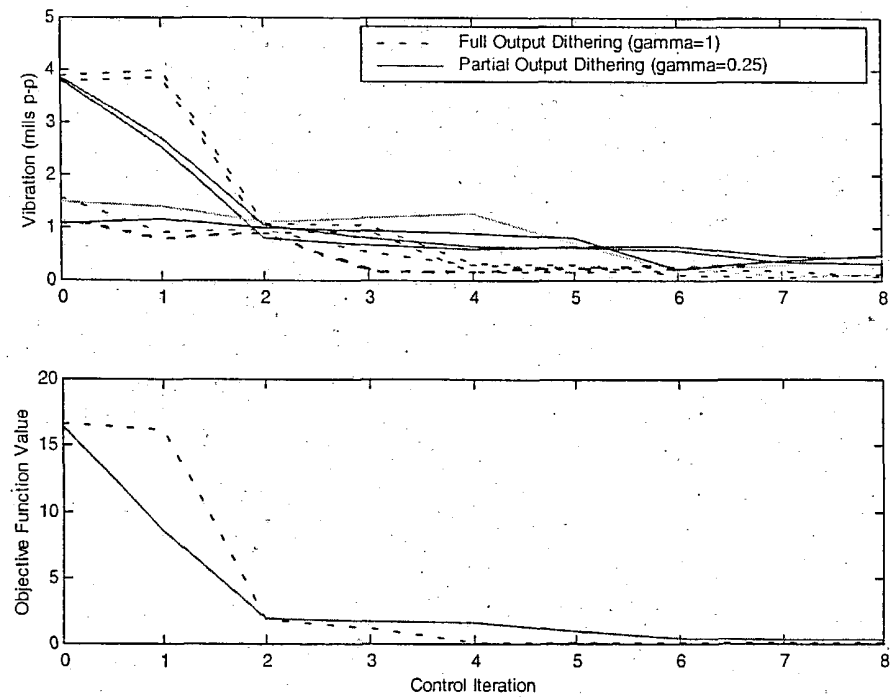


Figure 5.7 Results of Adaptive Optimal Control of Lightly Cross-Coupled System Using Full and Partial Control Dithering

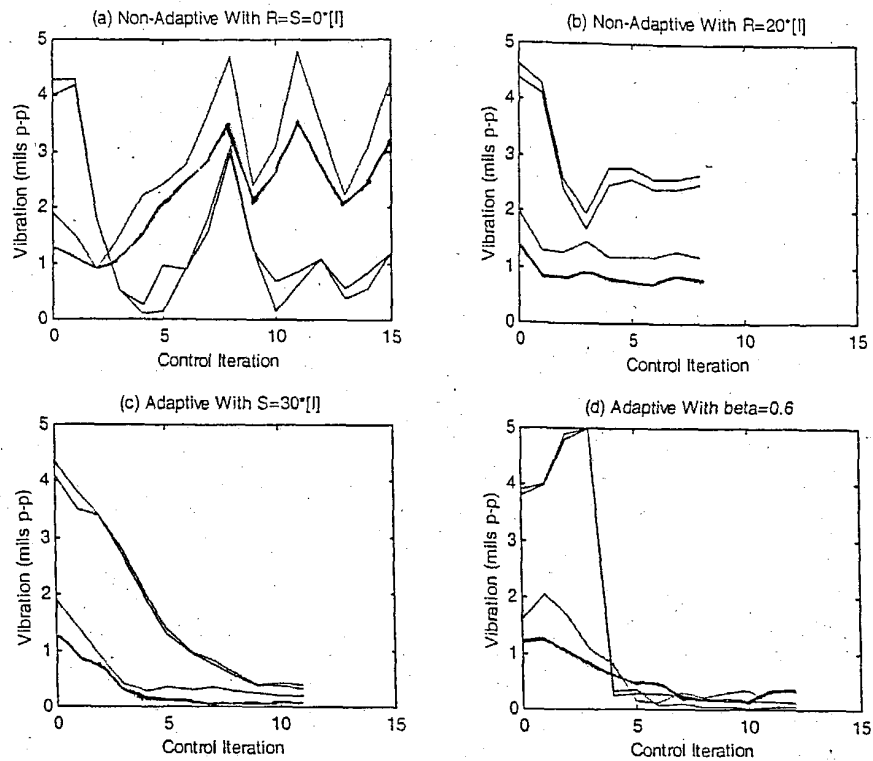


Figure 5.8 Dual-Plane Optimal Active Balancing Control Results for Somewhat Inaccurate Initial Influence Matrix Estimate

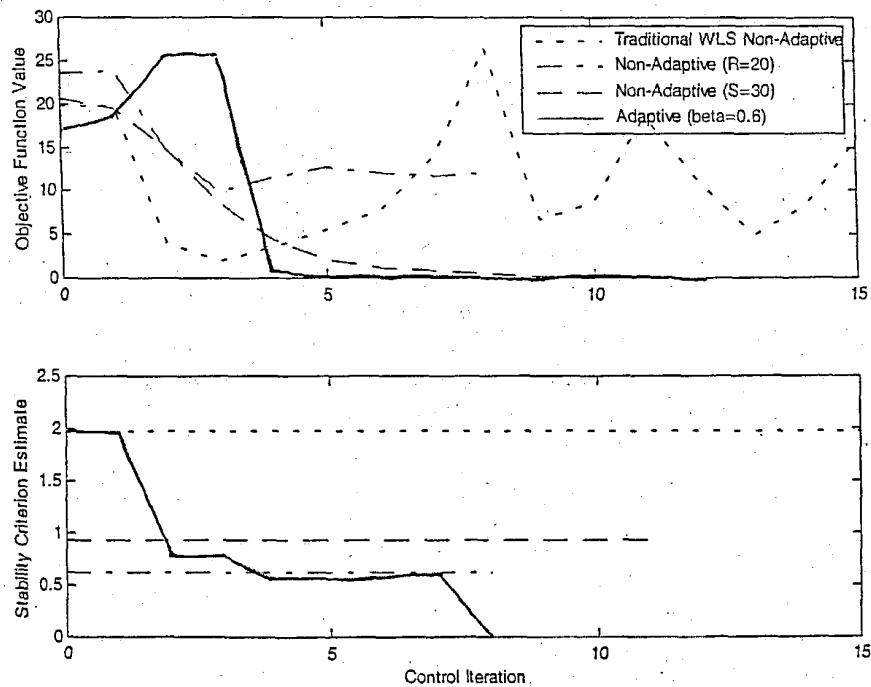


Figure 5.9 Objective Function Response and Estimated Stability Criterion During Optimal Active Balancing Control With Moderately Inaccurate Initial Influence Matrix Estimate

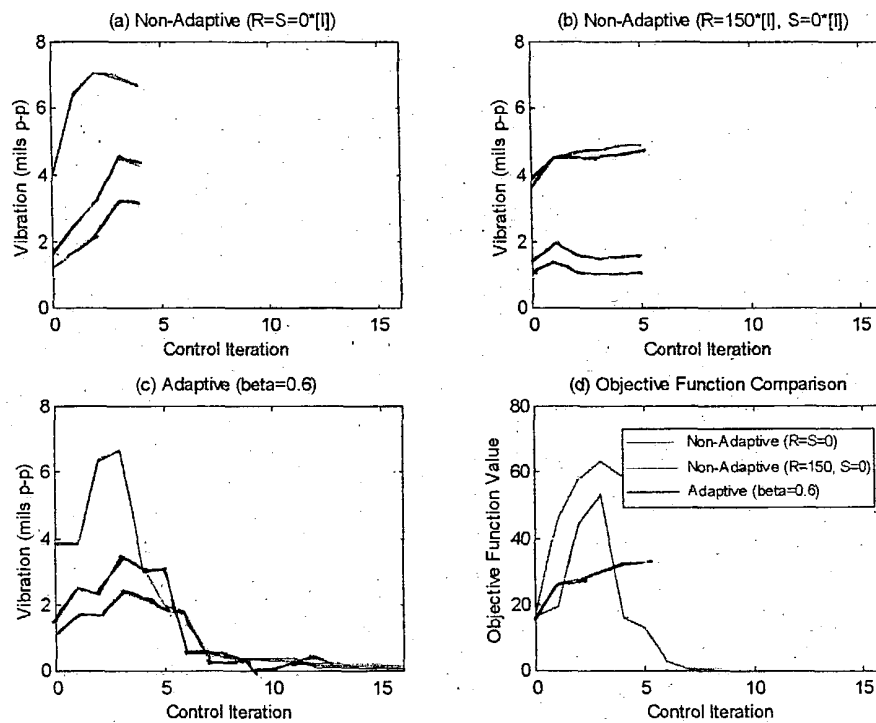


Figure 5.10 Results Of Non-Adaptive And Adaptive Optimal Control With Highly Inaccurate Influence Matrix Estimate